Lasers in Manufacturing Conference 2023

Spatially resolved temperature field measurement in powder bed fusion for online detection of porosity

Dieter Tyralla[a,*], Thomas Seefeld[a,b]

[a]*BIAS – Bremer Institut für angewandte Strahltechnik GmbH, Klagenfurter Straße 5, 28359 Bremen, Germany*
[b]*MAPEX Center for Materials and Processes – University of Bremen, Bibliothekstraße 1, 28359 Bremen, Germany*

Abstract

As many quality issues in powder bed fusion (PBF) may be related back to processing issues, there is a strong demand for online process monitoring that allows for a complete documentation of the AM build-up processes, and preferably an in-situ detection of imperfections like porosity.
Thermal monitoring with a 2-color thermal camera allows for a determination of melt pool dimensions with high lateral resolution during PBF. From this, a correlation of online melt pool size data and built density was established. A spatially resolved temperature field measurement with a frame rate of 500 Hz enables the layer wise evaluation of melt pool geometry with a spatial resolution of 9 µm within the entire build-up area of 250 mm by 250 mm. This method ensures a continuous process monitoring of the entire build-up process and enables the recognition of deviations in process behavior. For the first time, a correlation of these online monitoring data with spatially resolved porosity distribution data from micro-X-ray tomography measurements is established, indicating the potential of online porosity detection and monitoring in PBF.

Keywords: additive manufacturing, laser pwoder bed fusion, process monitoring, temperature measurement, porosity

1. Introduction

LPBF is a layer wise production technique that enables the manufacturing of metallic parts with complex 3-dimensional geometry. The part density is one of the most important properties in LPBF because of the influences on mechanical properties. Often, the density of the printed parts must be checked by destructive testing or a cost expensive non-destructive CT-measurement to prove their properties.

* Corresponding author. Tel.: +49-421-218-58000; fax: +49-421-218-58063.
E-mail address: info@bias.de.

The part density depends on a large number of process parameters like laser power, welding speed and layer thickness, but it is also influenced by the part geometry which varies for each component. The individual observation of parameters is often not sufficient, so that deviations only become apparent through a multivariate analysis of several parameters (Stojanovic et al. 2016). A statement on the quality of the component can only be made after the end of the manufacturing process (Gobert et al., 2018).

Essentially, a high density is achieved for a suitable ratio of the energy introduced and the volume of metal to be melted. A high energy input leads to deep penetration which may generate keyhole related pores in the part. Lack of fusion might take place for low energy input. It is commonly known that the temperature field in the process zone indicates the energy balance and can be used to identify applicable parameters.

For process observation in laser additive manufacturing, (high-speed) cameras, spectrometers and thermal melt pool analyses are used, among other things, to improve the process knowledge (Megahed et al., 2019). Since recent time, in-situ X-ray observations can also be performed in individual laboratory facilities, although only short sequences are recorded and integration into commercial facilities is not realistic in the foreseeable future (Richter et al., 2019). In addition to such laboratory facilities, various equipment manufacturers already offer monitoring systems for their laser powder bed fusion systems. The main focus here is on optical and thermographic monitoring methods.

In the powder bed process, however, an optical measurement of the temperature is particularly challenging, since on the one hand the process zone is very small with a few 100 µm, but the installation space is very large with several 100 mm (Khairallah et al., 2016). These boundary conditions require a high number of pixels to resolve the tiny melt pools within the large build area (Lough et al., 2020). Otherwise, only a small region in the build area can be observed (Furumoto et al., 2014).

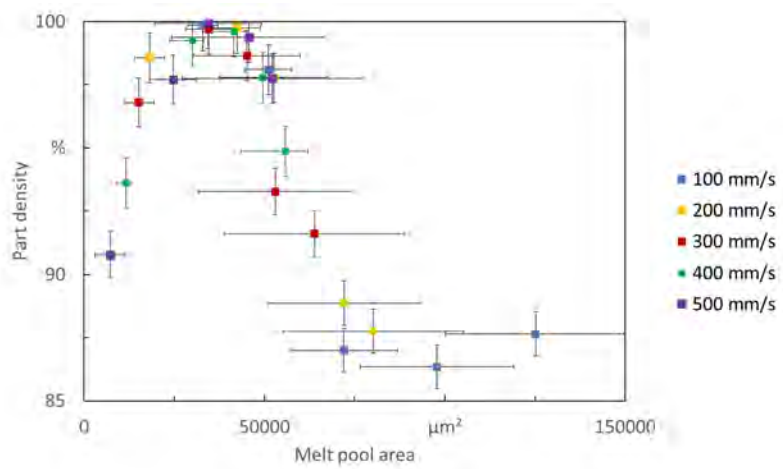

Fig. 1. Correlation of PyroCam measured melt pool area and corresponding part densityy for different process parameter (Tyralla et al., 2021)

The most common method for the temperature measurement in LPBF is a coaxial pyrometer measurement (Islam et al., 2013). In other cases, pyrometers in the near infrared range are integrated coaxially into the beam path (Forien et al., 2020). Here, the observation can be disturbed by spatter and powder that attenuates the process zone (Pavlov et al.; 2010). Thus, 2-channel pyrometers are preferred for the measurement. However, these sensors only provide single-spot temperature values (Gutknecht et al., 2020). The coaxial integration of

IR-cameras provides space-resolved temperature field information but is limited however because of the optical properties of common lenses and mirrors in LPBF.

A 2-channel-pyrometer camera enables the emissivity corrected temperature field measurement in other applications (Tyralla et al., 2020), and this approach was recently transferred to the LPBF process (Tyralla et al. 2021). A correlation between the overall part density and the online determined average melt pool size could be achieved, like shown in figure 1.

2. Experimental & methodology

A commercial LPBF machine (Realizer SLM 250) is used for the investigation. The build-up volume is 250 mm by 250 mm by 300 mm. A single-mode fiber laser provides a maximum laser power of 200 W at a wavelength of 1070 nm. The laser spot diameter measured by 2nd-momentum method is 50 µm. 20 mm thick steel plates of 1.0570 are used as substrate. In the present work, 316L is used as powder material with a particle size distribution between 15 µm and 45 µm.

A 2-channel-pyrometer camera (PyroCam, IMS Chips) is used for online temperature field analysis. The camera compares the radiation at 661 nm and 667 nm for an emissivity corrected temperature measurement between 650 °C and 1900 °C. The camera is integrated coaxially into the beam path by the help of a beam splitter like illustrated in fig. 2. The mirrors of the scanner unit are coated for higher reflectivity for laser radiation at 1070 nm and thermal radiation at 650 nm to ensure simultaneous processing and measurement. In addition, a special F-θ lens is used for high transmission in the mentioned spectral ranges, too. The camera manufacturer calibrates the PyroCam for the entire optical path. The accuracy is specified with 2%. This method ensures a process monitoring that follows the laser movement during build up with high frequency and enables the observation of the immediate area around the melting process with high resolution.

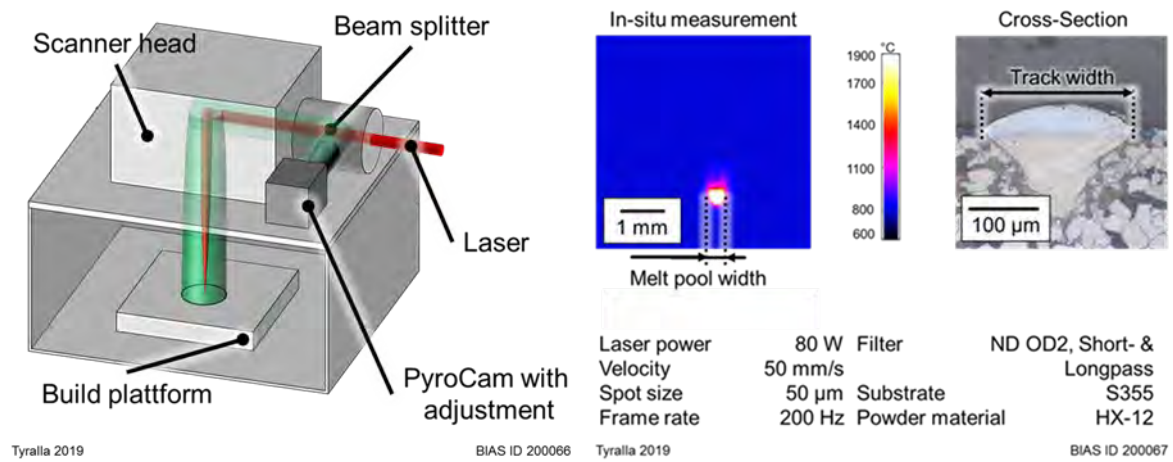

Fig. 2. Schematic of experimental set-up (left) and evaluation of PyroCam images (right). Comparison of PyroCam measured melt pool size and cross-section track width (Tyralla et al., 2021).

A LabView based evaluation algorithm is used for thermal image processing. The melt pool geometry is determined due to the detection of a bright area in each image that exceeds the melt temperature of the powder material of 1260 °C. The melt pool width, the length and the size are employed as thermal indicators for the process like shown in fig. 2. A detailed description of the setup is given in (Tyralla et al., 2021).

Images at different positions in the build-up area are taken to determine the lateral resolution of the camera and to calculate the effect of chromatic aberration. Furthermore, a validation of the thermal

calibration is done for the used optical setup by a blackbody radiator for a temperature range between 1200 °C and 1300 °C. The calibration source holds the set temperature to within 1 °C.

In this work, a frame rate of 500 Hz was used. The work investigates the influence of typical process parameters like laser power and welding speed on part density and melt pool size. Figure 3 shows the model and the hatch strategy of the printed part. Furthermore, the scanner position of the LPBF machine was tracked during the build-up process. Both data are linked to obtain a 3-dimensional heat map of the printed part.

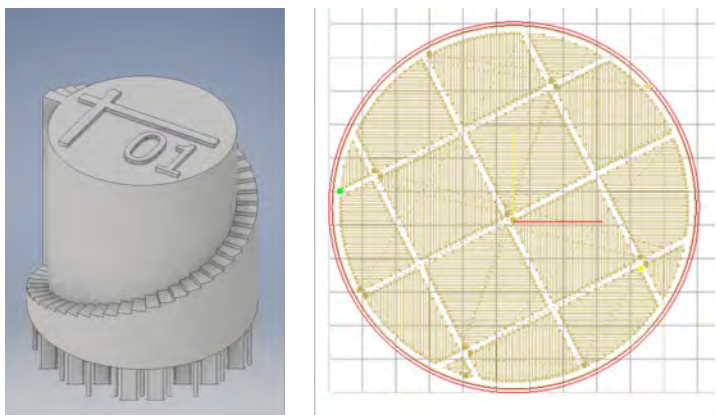

Fig. 3. Model of sample geometry and the hatch strategy. The layer height is 50 µm. The hatches of one layer are made up of patches of 3 mm by 3 mm. At the end of a layer the contour is welded. The welding direction is rotated by 79 ° for the next layer.

3. Results

Often, a wide range of parameter is investigated, resulting in very poor density values that are of no interest for typical applications. Thus, the parameter space was significantly reduced in the present work. A higher resolution should show how strong the correlation is between density and melt pool size and how large the density differences in the component must be for the monitor to still detect them. Finer gradations of the laser power allow a more precise determination of the optimum range of melt pool size and the resulting maximum density, as shown in fig. 4.

For each welding speed, there is a melt pool size range in which the density becomes maximum. This range shifts to higher values for increasing feed rates.

a)

	100 mm/s	200 mm/s	300 mm/s	400 mm/s	500 mm/s
200 W			95,9	96,4	97,5
190 W					
180 W					
170 W		95,4	95,1	96,5	98,0
160 W					
150 W		94,2			
140 W	94,2		96,8	98,0	98,0
130 W					
120 W	94,4	97,3			
110 W			98,0	96,5	95,4
100 W	98,1				
90 W		98,9			
80 W	99,4		96,6	95,1	93,7
70 W					
60 W	97,4	95,0			

b)

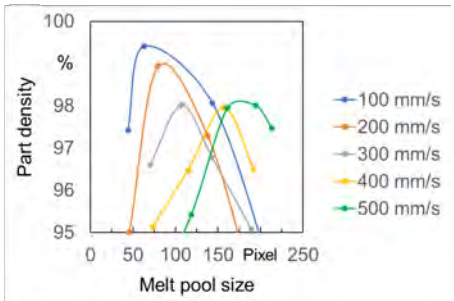

c)

100 mm/s		200 mm/s		300 mm/s		400 mm/s		500 mm/s	
[W]		[W]		[W]		[W]		[W]	
100	97,08	120	96,40	140	96,50	160	97,19	190	98,00
95	98,62	110	98,52	130	98,31	150	98,30	180	98,36
90	99,58	100	99,18	120	98,95	140	98,69	170	98,77
85	99,75	90	99,45	110	98,67	130	98,26	160	98,73
80	99,63	80	99,21	100	97,87	120	97,45	150	98,37

d)

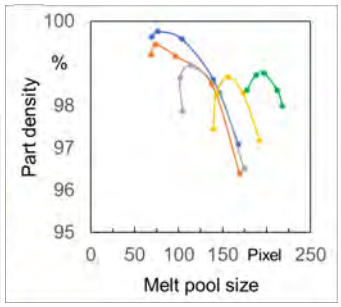

Fig. 4. Process parameter and corresponding part density value with 316L for a) & b) a large parameter space and with c) & d) a finer gradation. a) and c) show the chosen process parameter. b) & d) show the correlation of part density value and the measured melt pool size.

While the density maxima for 100 mm/s and 200 mm/s are between 70 pixels and 80 pixels, it shifts to values between 100 pixels and 120 pixels for 300 mm/s. For 400 mm/s, the density maximum is between 150 pixels and 160 pixels. For 500 mm/s, it is between 180 pixels and 200 pixels. The values are summarized in Table 1.

Table 1. Optimum melt pool size depending on welding speed.

Welding speed	Melt pool size of maximum density [Pixel]
100 mm/s	73,9
200 mm/s	76,3
300 mm/s	114,1
400 mm/s	155,8
500 mm/s	195,1

The frame rate of the camera of 500 Hz leads to about one million melt pool size values per printed part. For the analysis of the results shown above, all these data of the online monitoring system of one printed part were averaged into only one melt pool size value that would be correlated to one part density value obtained with the Archimedes measurement method.

Now, in order to fully exploit the capability of the online monitoring system, the individual values are evaluated layer-wise in the next step of investigation. Fig. 5a shows the melt pool size for different parameter combinations resolved layer-wise. It can be seen that the melt pool size varieties depending on the position

in the printed part. For 100 mm/s, the melt pool size slightly increases with the number of layer whereas it strongly decreases for higher welding speeds like 300 mm/s and 500 mm/s. It can be assumed that heat conduction plays an important role for the melt pool size. The plots also show the density values of Archimedean measurement for the whole printed part.

The so far achieved results would suggest that each melt pool value correlates to a certain density. Data points with the same melt pool size level should have the same density value. Therefore, µ-CT-scans are applied on the printed parts. The scan data enables a detailed evaluation of the inner structure and obtain density values from different positions within the printed part. The scan data are sliced in x-y-direction to generate slices with the maximum resolution of the system, here, 15 µm. Each slice was evaluated regarding its greyscale to get the porosity at the corresponding position like shown in fig. 5b. The slices are averaged to get one value for each individual layer like shown in fig. 5c. For 100 mm/s, the graphs are close together. In case of 300 mm/s and 500 mm/s the density strongly variates. The graphs demonstrate a dependency of density on the position in the part for all parameter combinations as was already the case with the previous results of melt pool size.

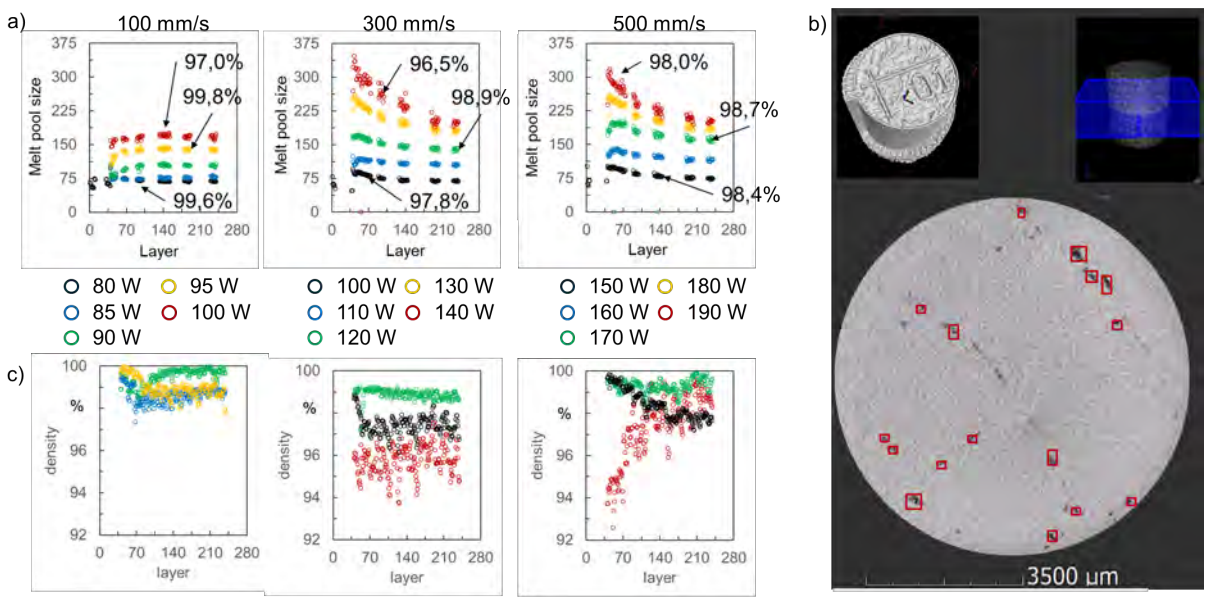

Fig. 5. a) melt pool size as function of the layer number. A strong dependency can be observed for higher welding speeds. b) evaluation method of µ-CT-Scan data. Here, the average grayscale of each slice is evaluated to get the density as a function of the layer number. c) Density as function of the layer number. The values are determined by an evaluation of CT-scans.

In the next step, the individual melt pool values within the layers were considered. In order to achieve a possible correlation between melt pool size and density at x-y-z-position of the printed part or even the assignment of a conspicuous melt pool value to a defect location, the temperature data must first be assigned to a specific position in the printed part. Since the scan vectors in the LPBF are usually very complex, the scanner position was recorded directly in the process using a high frequency measurement. Using the time stamp of the two data sets, temperature data and scanner position could be linked. Fig. 6a shows the scanner path along the hatch strategy and the allocated melt pool size values for one layer.

This allocation enables within each layer the identification of local deviations of the melt pool size and singularities in the process behavior, including hot spots and regions with lower-than-average temperatures,

both of which might potentially indicate sites of porosity formation.

Fig. 6b shows a typical example of a "melt poos size map" indicating a hot spot at the starting point of the layer, as well as several cold spots that also appear to coincide with the pattern of the applied hatching strategy.

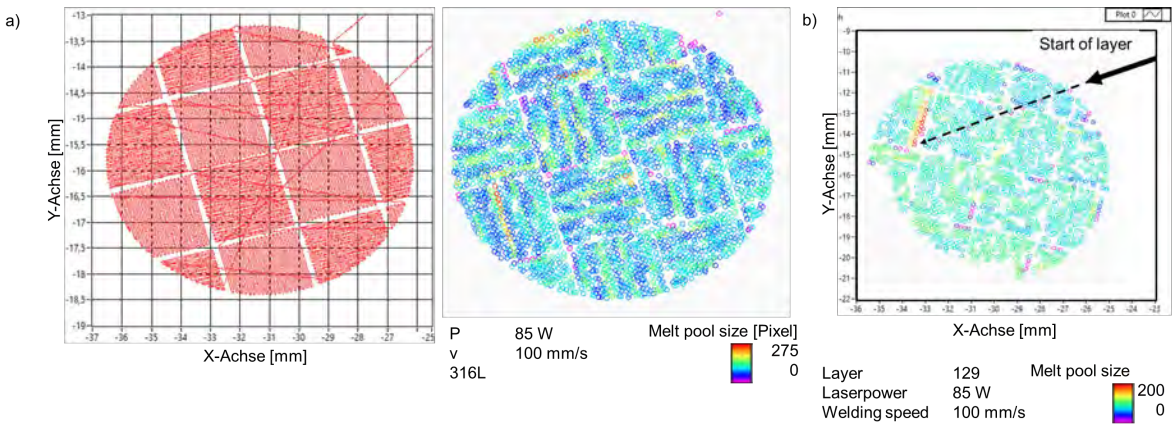

Fig. 6. a) High frequency measurement of the scanner position in one layer and its corresponding melt pool values. b) evaluation of melt pool sizes in layer 129. Here, the melt pool starts with a significantly higher value that could result from bad parameter or hatch strategy.

The next step in this analysis describes the stacking of the individual layers into a 3-dimensional representation of the part. Fig. 7a shows the stacked melt pool maps of 100 mm/s with different laser power. The melt pool size shifts to higher values indicated by the color. Fig. 7b shows a typical example of a "3-dimensional melt poos size map" indicating a higher level of melt pool size on the left side that appear to coincide with the position in the build area. Here, the part was printed very close to the edge of the building platform.

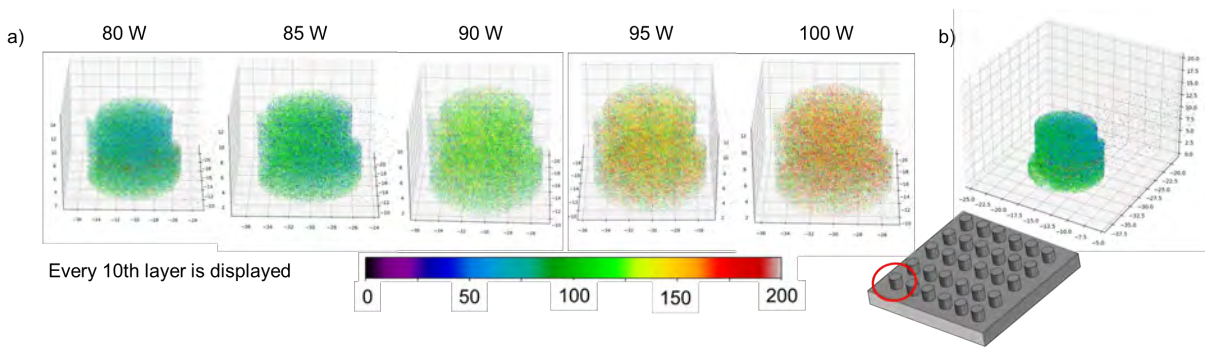

Fig. 7. a) stacked melt pool size values for the hole printed part. Only every 10th layer is displayed. b) evaluation of stacked melt pool size representation. Here, the left side of the part shows a higher level of melt pool size values which is possibly due to the position of the printed part within the build area, located near to the corner of the build platform.

4. Discussion

There are results of a previous study (Tyralla et al., 2020), where the frame rate was 200 Hz. Compared to this, the new result with a higher frame suggests that the frame rate could have an influence on the quality of the data. It can be assumed that higher frame rates increase the accuracy of melt pool observation, like shown in fig. 8. Here, the track width is compared to the melt pool width of single welding track experiments. The image show that the accuracy is improved for the higher frame rate. Here, up to 100 mm/s the deviation is 3% for 200 Hz and 3% up to 200 mm/s for 500 Hz, respectively.

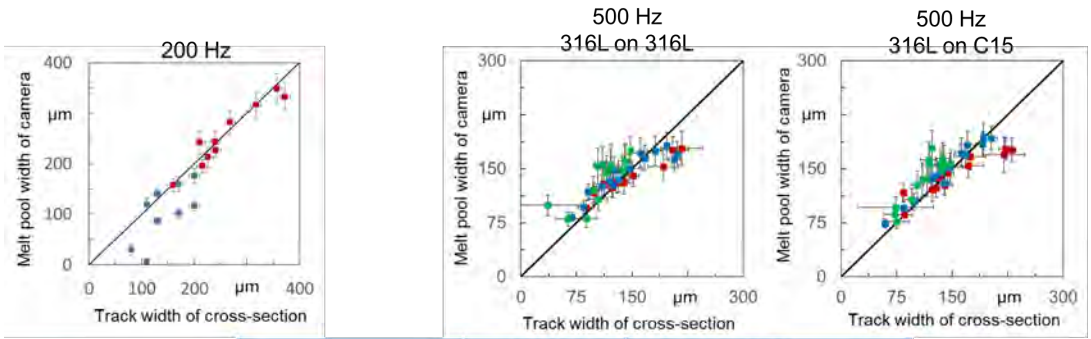

	200 Hz	500 Hz	
Ava. deviation	HX-12 on S355	316l on 316L	316l on C15
100 mm/s	3%	4%	5%
200 mm/s	15%	3%	5%
300 mm/s	35%	18%	15%
400 mm/s	-	22%	16%
500 mm/s	-	19%	16%

Fig. 8. Comparison of track width and melt pool width measured in cross-section and camera, respectively.

An online temperature measurement system was used to determine the melt pool size during the build-up process. The values are recorded with a high framerate of 500 Hz. The values are averaged and correlated to the density of the corresponding part which was determined by Archimedean method. The results show a correlation between melt pool size and part density that depends on the welding speed. There is one distinct maximum of density for each welding speed. Fig. 9a show the correlation of density and melt pool size for all parameter variations. The different laser power-welding speed combinations for the different parameter variations are marked with dashed lines. Here, the range of the maximum density is located at the same melt pool size for all welding speeds. The values correspond to the melt pool sizes shown in table 1.

Whereas the correlation is very clear for 100 mm/s, the dashed lines differ in height for the higher welding speeds. It can be assumed that the differences for higher welding speeds can be attributed to the evaluation method where melt pool sizes for the whole part are averaged and density values are determined by Archimedes measurement method. It appears that the strong dependency of the melt pool size on geometry for higher welding speeds (see fig. 5) interfere a clear correlation.

Therefore, a novel approach was chosen which evaluates the melt pool sizes and the density for single layers of the printed part. This method uses CT-scan data which are sliced and analyzed layer-wise to generate density values depending on layer number. In addition, the monitoring data are averaged for each layer to generate melt pool values depending on layer number. In order to check whether a clear correlation is possible

for all parameters and welding speeds, the melt pool and density are now correlated for the single layers, as was previously done at the part level. The correlation is shown in fig. 9b.

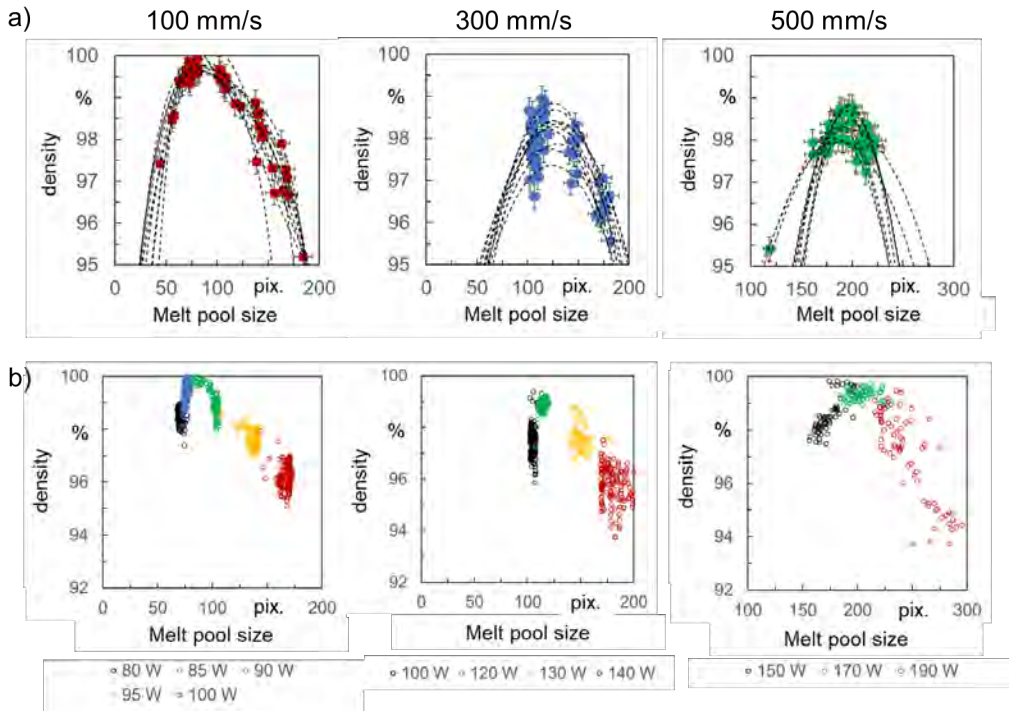

Fig. 9. a) correlation of density and melt pool size. Each point is one part. The values for one part are averaged. The melt pool range for maximum density is located on the same position for single welding speeds. The maxima of density differ for higher welding speeds. b) correlation of density and melt pool size for one printing job. Each color represents one part with its about 200 layers. Here, the correlation is clear for all welding speeds.

Furthermore, in an additional step, the scanner position was measured during process and the melt pool size was allocated to the corresponding scanner position. Thus, 3-dimensional melt pool maps can be created which potentially enable the analysis of individual singularities within the part, if the data can be correlated to CT-data. The allocation and evaluation of individual welding defects with online monitoring data are very demanding.

5. Conclusion

A temperature measurement system was integrated on-axis into a commercial LPBF machine. The 2-channel-pyrometer method ensures emissivity corrected temperature field measurement with a frame rate of 500 Hz. The lateral resolution is less than 0.010 mm in the entire build area of 250 mm by 250 mm. The thermal accuracy was verified by a blackbody and the deviation is 1.7% in the temperature range of interest.

A correlation between melt pool size and density is demonstrated on level of the hole part which imply a optimum range of melt pool size for maximum density of the part. The evaluation of each single layer of the printed part shows a strong dependency of melt pool size on the position in the part. A layer-wise evaluation of density was performed by CT-scans that confirm a comparable dependency for density. The layer-wise evaluation could explain existing inaccuracies of the previously used part-based correlation.

The HF measurement of the scanner position enables the allocation of melt pool size on x-y-z-position within the part. Thus, two and three-dimensional melt pool size maps can be generated which potentially enable the allocation of regions with lower/ higher-than-average temperatures to singularities in the part.

Acknowledgements

The work was funded by the Bremer Luft- und Raumfahrtfroschungsprogramm 2020 under contract no. LURAFO3001C from funds of the European Union, of the European Regional Development Fund and the state of Bremen, which the authors gratefully acknowledge.

References

Stojanovic, L.; Dinic, M.; Stojanovic, N.; Stojadinovic, A. (Hg.) (2016): Big-data-driven anomaly detection in industry (4.0): An approach and a case study. 2016 IEEE International Conference on Big Data (Big Data). 2016 IEEE International Conference on Big Data (Big Data).

Megahed, M. et al. (2019): LPBF Right the First Time—the Right Mix Between Modeling and Experiments. In: Integrating Materials and Manufacturing Innovation 8 (2), S. 194–216. DOI: 10.1007/s40192-019-00133-8.

Richter, B. et al. (2019): High-speed X-ray investigation of melt dynamics during continuous-wave laser remelting of selective laser melted Co-Cr alloy. In: CIRP Annals 68 (1), S. 229–232. DOI: 10.1016/j.cirp.2019.04.110

Khairallah, S.A., Anderson, A.T., Rubenchik, A., King, W.E., "Laser powder-bed fusion additive manufacturing: Physics of complex melt flow and formation mechanisms of pores, spatter, and denudation zones", Acta Materialia 108, 2016, 36-45

Forien, J.-B., Calta, N. P., DePond, P. J., Guss, G. M., Roehling, T. T., Matthews, M. J., 2020. Detecting keyhole pore defects and monitoring process signatures during laser powder bed fusion: A correlation between in situ pyrometry and ex situ X-ray radiography, Additive Manufacturing Vol.35, 101336. DOI: 10.1016/j.addma.2020.101336.

Furumoto, T., Ueda, T., Alkahari, M., Hosokawa, A., 2013. Investigation of laser consolidation process for metal powder by two-color pyrometer and high-speed video camera, CIRP Annals - Manufacturing Technology 62, p.223–226.

Gobert, Christian; Reutzel, Edward W.; Petrich, Jan; Nassar, Abdalla R.; Phoha, Shashi (2018): Application of supervised machine learning for defect detection during metallic powder bed fusion additive manufacturing using high resolution imaging. In: Additive Manu-facturing 21, S. 517–528. DOI: 10.1016/j.addma.2018.04.005.

Gutknecht, K., Haferkamp, L., Cloots, M., Wegener, K., 2020. Determining process stability of Laser Powder Bed Fusion using pyrometry, Procedia CIRP Vol.95, p. 127-132, DOI: 10.1016/j.procir.2020.01.147.

Islam, M., Purtonen, T., Piili, H., Salminen, A., Nyrhila, O., 2013. Temperature profile and imaging analysis of laser additive manufacturing of stainless steel, Physics Procedia 41, p. 835 – 842

Lough, C.S., Wang, X., Smith, C.C., Landers, R.G., Bristow, D. A., Drallmeier, J.A., Brown, B., Kinzel, E.C., 2020. Correlation of SWIR imaging with LPBF 304L stainless steel part properties, Additive Manufacturing Vol. 35, 101359. DOI: 10.1016/j.addma.2020.101359.

Pavlov, M., Doubenskaia, M., Smurov, I., 2010. Pyrometric analysis of thermal processes in SLM technology, Physics Procedia 5, p. 523–531.

Tyralla, D.; Köhler, H.; Seefeld, T.; Thomy, C.; Narita, R., 2020. A multi-parameter control of track geometry and melt pool size for laser metal deposition. In: Procedia CIRP 94, p. 430-435

Tyralla, D., Seefeld, T., 2021. Thermal Based Process Monitoring for Laser Powder Bed Fusion (LPBF), Advanced Materials Research Vol. 1161, p. 123-130. DOI: 10.4028/www.scientific.net/AMR.1161.123